Computational analysis of solar light harvesting properties of TiO2-BiVO4 inverse opals for applications in photocatalysis

Habli, Omayma; Lourdu Madanu, Thomas; Su, Bao Lian; Deparis, Olivier

Published in:
Journal of Energy Chemistry

DOI:
10.1016/j.jechem.2025.09.035

Publication date:
2026

Document Version
Publisher's PDF, also known as Version of record

Journal of Energy Chemistry 113 (2026) 610–621

Contents lists available at ScienceDirect

Journal of Energy Chemistry

journal homepage: www.elsevier.com/locate/jechem

http://www.journals.elsevier.com/journal-of-energy-chemistry/

Computational analysis of solar light harvesting properties of TiO_2-$BiVO_4$ inverse opals for applications in photocatalysis

Oumayma Habli [a], Thomas L. Madanu [b,c], Bao-Lian Su [b,d,*], Olivier Deparis [a,*]

[a] Namur Institute of Structured Matter, University of Namur, 61 Rue de Bruxelles, 5000 Namur, Belgium
[b] Laboratory of Inorganic Materials Chemistry (CMI), University of Namur, 61 rue de Bruxelles, Namur B-5000, Belgium
[c] Department of Organic Chemistry, Loyola Academy, Old Alwal, Secunderabad, Telangana 500010, India
[d] State Key Laboratory of Advanced Technology for Material Synthesis and Processing, Wuhan University of Technology, Wuhan 430070, Hubei, China

ARTICLE INFO

Article history:
Received 10 June 2025
Revised 1 September 2025
Accepted 7 September 2025
Available online 27 September 2025

Keywords:
Inverse Opal
RCWA method
Slow photon
TiO_2
$BiVO_4$
Photocatalysis
Light harvesting

ABSTRACT

Efficient solar light harvesting is essential for high-performance photocatalysts. Here, Rigorous Coupled-Wave Analysis (RCWA) computational method is used to investigate and optimize the optical absorption of TiO_2-$BiVO_4$ inverse opal (IO) structures under varying light incidence angles and pore-filling medium (air or water). Simulations were validated against experimental reflectance data. They revealed that small-pore IOs strongly absorb in the UV-C and UV-B regions due to the slow photon effect, making them ideal for sterilization and water disinfection. Medium- and large-pore IOs benefit from additional slow photon effect at the 2nd order photonic band gap, enhancing absorption across both UV and visible regions. Medium-pore IOs are suited for indoor air treatment and water purification, while large-pore IOs with the highest photon flux enhancement enable solar-driven photocatalysis such as outdoor pollutant removal and hydrogen production. For all tested IO designs, the absorbed photon flux exceeds that of equivalent planar slabs, highlighting the advantage of photonic structuring for sustainable photocatalytic applications.

1. Introduction

The development of efficient photocatalytic materials is crucial for addressing global challenges in renewable energy and environmental remediation [1,2]. Among these materials, titanium dioxide (TiO_2) has been widely studied as photocatalyst [3,4] due to its strong oxidative capabilities, high chemical stability, and low cost [5]. TiO_2 exists in anatase, rutile and brookite phases, among which anatase is the most used in degrading a wide range of organic pollutants and generating hydrogen under UV light [6]. However, its wide electronic bandgap (~3.2 eV) limits the absorption of light primarily to the ultraviolet (UV) region, which represents only a small fraction of the solar spectrum, thereby restricting its efficiency under natural sunlight [7]. Moreover, its photocatalytic activity is further hindered by the rapid recombination of photogenerated electron-hole pairs, which significantly reduces overall efficiency [8]. To overcome limitations, various strategies have been employed to extend TiO_2 photo-response into the visible region. Doping with metal and non-metal elements has been shown to enhance light absorption in the visible region [9,10]. Additionally, coupling TiO_2 with narrow bandgap semiconductors, such as bismuth vanadate ($BiVO_4$), has been explored to improve charge separation, thereby reducing electron-hole recombination, and enhance photocatalytic activity under visible illumination [11,12]. $BiVO_4$, with a bandgap of ~2.4 eV, can absorb visible light efficiently, but performance of $BiVO_4$ catalysts is hindered by poor electron mobility and short carrier diffusion lengths typically around 70–100 nm which limit effective charge transport and increase recombination [13]. Alongside its synergetic action with TiO_2 in photocatalysis, bismuth vanadate has also been widely used as photoanodes for photoelectrochemical (PEC) water splitting. For example, constructing hetero-interfacial hybrid photoanodes with FeOCl [14] or integrating $BiVO_4$ with metal-organic frameworks [15] have led to substantial improvements in PEC performance. Morphology control and interface engineering have

* Corresponding authors. Laboratory of Inorganic Materials Chemistry (CMI), University of Namur, 61 rue de Bruxelles, Namur B-5000, Belgium (B-L. Su); Namur Institute of Structured Matter, University of Namur, 61 Rue de Bruxelles, 5000 Namur, Belgium (O. Deparis).

E-mail addresses: omayma.habli@unamur.be (O. Habli), bao-lian.su@unamur.be (B.-L. Su), olivier.deparis@unamur.be (O. Deparis).

https://doi.org/10.1016/j.jechem.2025.09.035
2095-4956/

contributed to produce highly efficient $BiVO_4$-based photoanodes [16]. These studies highlight $BiVO_4$ versatility as a visible-light-responsive semiconductor for environmental remediation and solar-driven chemical transformations, reinforcing its synergy with TiO_2 for efficient photocatalysis.

In the literature, the band alignment between TiO_2 and $BiVO_4$ is facet-dependent and governs charge separation. TiO_2 (101)/$BiVO_4$ (010) forms a Type I junction with negligible valence band offset, confining carriers within $BiVO_4$ and favoring recombination [17]. In contrast, TiO_2 (101)/$BiVO_4$ (110) interface adopts a Type II alignment, driving electrons from the conduction band (CB) of $BiVO_4$ to the CB of TiO_2 and vice versa for holes. This interface shows superior photocatalytic activity compared with the Type I $BiVO_4$ (010)-TiO_2 system [18]. Although our XRD could not resolve the exposed $BiVO_4$ facet [19], drawing on previous theoretical and experimental studies [17,18,20,21] and our observed photocatalytic performance, we infer that a type II heterojunction is the most plausible mechanism for efficient charge separation and transfer (see Fig. S1, Supplementary Information).

Long-term photostability of $BiVO_4$ is another crucial factor to consider, besides interfacial band alignment. Although $BiVO_4$ is prone to photocorrosion, in our TiO_2-$BiVO_4$ IO composite system, several synergistic factors act to suppress this undesirable process. From a thermodynamic perspective, the valence band edge of $BiVO_4$ lies at ~+2.4 V vs. NHE, positive enough to drive Bi^{3+} self-oxidation. However, RhB and its degradation fragments possess much lower oxidation potentials (<+1.2 V vs. NHE). Hence, hole-driven oxidation of RhB is strongly favored over $BiVO_4$ oxidation, ensuring that photogenerated holes preferentially degrade RhB rather than attack the $BiVO_4$ lattice. Beyond thermodynamics, the TiO_2-$BiVO_4$ heterojunction promotes efficient charge separation, suppressing electron-hole recombination and reducing hole accumulation in the $BiVO_4$ valence band [20]. This process is further enhanced by strong interfacial interaction between the composite and RhB, as evidenced by low contact angles reported in our earlier study [22]. The IO morphology of TiO_2-$BiVO_4$ composite also contributes significantly. Its interconnected porous framework provides high surface area and short carrier transport distances, ensuring rapid transfer of photogenerated holes to RhB molecules or, in water oxidation, to H_2O. This minimizes localization of holes at $BiVO_4$ lattice sites where photocorrosion could occur [23] Finally, because RhB is present in large excess relative to $BiVO_4$ active sites, it acts as an abundant sink for photogenerated holes, further reducing the chance of self-oxidation. Together, these factors ensure that photogenerated holes are rapidly and preferentially utilized in the oxidation of RhB (or water molecules in water-splitting applications), thereby stabilizing $BiVO_4$ against photocorrosion.

Apart from electronic interactions, structural designs play an important role in influencing photocatalytic performance. A promising strategy to enhance light absorption and photocatalytic performance involves modifying the morphology of the photocatalyst into periodically ordered photonic structures, which exhibit unique optical properties, including 'photonic band gap' and 'slow photon effect' [24]. At the edges of the photonic band gap (PGB), slow photons—light waves with vanishing group velocity—extend the optical path length and strengthen light-matter interactions, thereby increasing photon absorption. This enhanced light harvesting promotes more efficient charge carrier generation, ultimately improving photocatalytic activity [25,26]. Among different photonic structures, inverse opal (IO) photonic crystals have gained significant interest due to their ease of fabrication, highly ordered 3D porous architecture and tunable photonic bandgaps [27].

Recent studies have demonstrated that TiO_2 inverse opals coupled with visible-light-responsive semiconductors like $BiVO_4$, can significantly enhance photocatalytic activity under solar irradiation [19]. This enhancement is attributed to the synergistic effects of light absorption, efficient charge separation, and the unique photonic properties of the IO structure. For instance, Madanu et al. reported that the photocatalytic activity (degradation of Rhodamine B) of $BiVO_4$ in IO TiO_2 structures, promoted by the slow photon effect [19,22], exhibited up to a sevenfold enhancement compared to non-structured films. Previously, ordered macroporous TiO_2/$BiVO_4$ nanocomposites were shown to provide larger active surface areas and increased mass transfer, leading to high photocatalytic activity under visible light irradiation [11].

The slow photon effect relies on the ability to tune the PBGs of these IO structures by varying parameters such as the lattice spacing constant (pore size), the volume filling fraction of the dielectric medium and the light incidence angle. Since the first report on the application of slow photon effect in photocatalysis in 2006 [28], the optimization of slow photon frequencies to match the electronic bandgap of the photocatalyst has been actively pursued to the present day [25,29,30].

Numerical simulations play an important role in the study of the optical properties of IO structures. Unlike experimental approaches, where absorptance measurement can be complicated and subject to uncertainties, simulations enable accurate prediction of this key parameter, which is directly correlated with photocatalytic performance. Moreover, they offer great flexibility by allowing the investigation of how structural parameters, such as sphere diameter, slab thickness, and volume filling fraction, influence the optical response of the material. While experimental studies can only test a limited set of sphere diameters, simulations can vary the diameter continuously, allowing the analysis of the PBG position relative to the electronic band edge of the material, thus optimizing the absorptance for photocatalysis. In this work, we focus on three representative diameters corresponding to IO samples that were fully characterized [22], enabling direct validation of our simulations. This choice ensures that our results are relevant to real IO structures while capturing features that guide their optimization. In addition, simulations can be used to analyze the reflectance and absorptance spectra at different incidence angles and azimuths, which is difficult to achieve experimentally. This theoretical approach not only provides a better understanding of photonic effects but also allows for the optimization of conditions to maximize the absorptance in specific spectral ranges, suitable for photocatalytic applications.

Different computational methods exist for full-vector three-dimensional calculation of the electromagnetic field in inverse opals. The Finite-Difference Time-Domain Method (FDTD) [31] has been applied to modelling of inverse opals, where the unit cell is discretized into voxels and periodic Bloch boundary conditions are used [32]. The Finite-Element Method (FEM) has been recently applied with same boundary conditions but using a tetrahedral mesh for unit cell discretization [33]. For inverse opal structures, especially those with a volume filling factor lower than close packing value (the present study), accurate discretization of the thin material skeleton requires a high number of voxels per unit cell (FDTD) or fine meshing (FEM), which burdens computational effort.

While experimental studies and numerical methods have advanced our understanding, accurate and efficient modeling of IO structures remains challenging. In this work, we used the Rigorous Coupled-Wave Analysis (RCWA) electromagnetic method to compute reflectance and absorptance spectra and deduce the harvested photons flux. First, we validate the accuracy of the method by comparing the calculated reflectance spectra with experimental results at different incidence angles. We then conduct a predictive analysis of absorptance and harvested photon flux within the inverse opal, investigating the influence of slow photon effect,

through angular-dependent absorptance, on photocatalytic performance. The specific advantage of this method is that the thin material skeleton geometry is described by a Fourier series decomposition in each layer. In our RCWA implementation (see Supplementary Information), the Fourier coefficients of the islands are calculated once for all and used in each iteration (wavelength or angle), which makes the computation very efficient when calculating spectral quantities (reflectance, absorptance). The accuracy of the material skeleton representation is determined by the number of Fourier coefficients, for which a trade-off must be found with computation time and memory.

Our findings provide new insights into the role of photonic effects in optimizing light harvesting in inverse opal structures, which is critical for improving efficiency in solar-driven photocatalytic applications.

2. Experimental

2.1. Composite inverse opals

The photonic structure under investigation is an inverse opal photonic crystal composed of a TiO_2-$BiVO_4$ composite. In previous experimental works [19,22], $BiVO_4$ was deposited as individual nanoparticles (NPs) on the walls of a TiO_2 skeleton (see Fig. 3a–c in [22]). However, these samples contained defects and imperfections. In contrast, the theoretical model employed here assumes a perfect IO slab, composed of an effective medium that approximates the actual TiO_2-$BiVO_4$ composite. The voids (pores) of the IO are modelled as filled with either air (refractive index: n = 1.0) or water (refractive index: n = 1.33).

Although in liquid phase photocatalytic experiments, the pores are filled with the analyte solution (e.g., 1.5 μM RhB solution in [22]), we choose air-filled pores for some simulations because it provides the strongest refractive index contrast between the skeleton material and the pore medium (i.e., air), thereby representing the most challenging case for assessing the accuracy of RCWA predictions. In addition, those simulations helped us to determine light harvesting and photocatalytic potential in air medium, as in the case of air remediation. Therefore, we compare the simulated reflectance spectra with those measured in pristine samples having pores filled with air (Fig. 1). In previous experiments [19,22], the volume filling fraction of TiO_2-$BiVO_4$ was estimated to be f = 0.12, which is lower than the close-packing value for an inverse opal (f = 0.26). As a result, the walls of the skeleton have open circular windows that interconnect adjacent pores (e.g., see Fig. 1a–c in [22]). For this study, we selected three TiO_2-$BiVO_4$ inverse opal (ITB) slabs with different spherical void diameters (D): 220 nm (ITB-220), 310 nm (ITB-310), and 340 nm (ITB-340), based on previous experimental works [19,22]. For efficient photoreactions, an open macroporous network (interconnected pores) is required, which is obtained by considering f = 0.12, as in experimental works.

Our theoretical analysis begins by considering a stack of inverse opal unit cells (Fig. S2, Supplementary Information) placed on a semi-infinite glass substrate (refractive index: n_{glass} = 1.50). The IO (face-centered cubic lattice) is assumed to be oriented such that the (1 1 1) crystallographic direction is perpendicular to the slab surface, as in [19]. Each IO unit cell contains three spherical voids (Fig. 1, inset). The slab consists of three IO unit cells ($N_{uc} = 3$) and the upper and lower unit cells are truncated so that the slab is terminated by full spheres, as in samples fabricated by self-assembly of templating spheres [19,22]. This corresponds to a total of eight (instead of nine) spheres per slab thickness (see Fig. S2, Supplementary Information). The experimental sample thicknesses are comparable to the theoretical ones (see Table S1, Supplementary Information).

The material absorption is accounted for by the imaginary part of the complex refractive index, i.e., the extinction coefficient k. The refractive index of the composite material was determined as $n_{mat} = x n_{TiO_2} + (1-x) n_{BiVO_4}$, where n_{TiO_2} and n_{BiVO_4} are the refractive indices of microporous TiO_2 and $BiVO_4$, respectively, while x and $(1-x)$ denote the corresponding volume fractions (see [22] for details about microporosity of TiO_2). The value of x = 0.88, determined previously [22], is assumed in this work. At λ = 500 nm, the real parts of the refractive indices of the individual components were derived as $n_{TiO_2} = 1.836$ and $n_{BiVO_4} = 2.764$ [22], based on calculations of the wavelength-dependent complex refractive index using data from dense TiO_2 [34] and $BiVO_4$ [35]

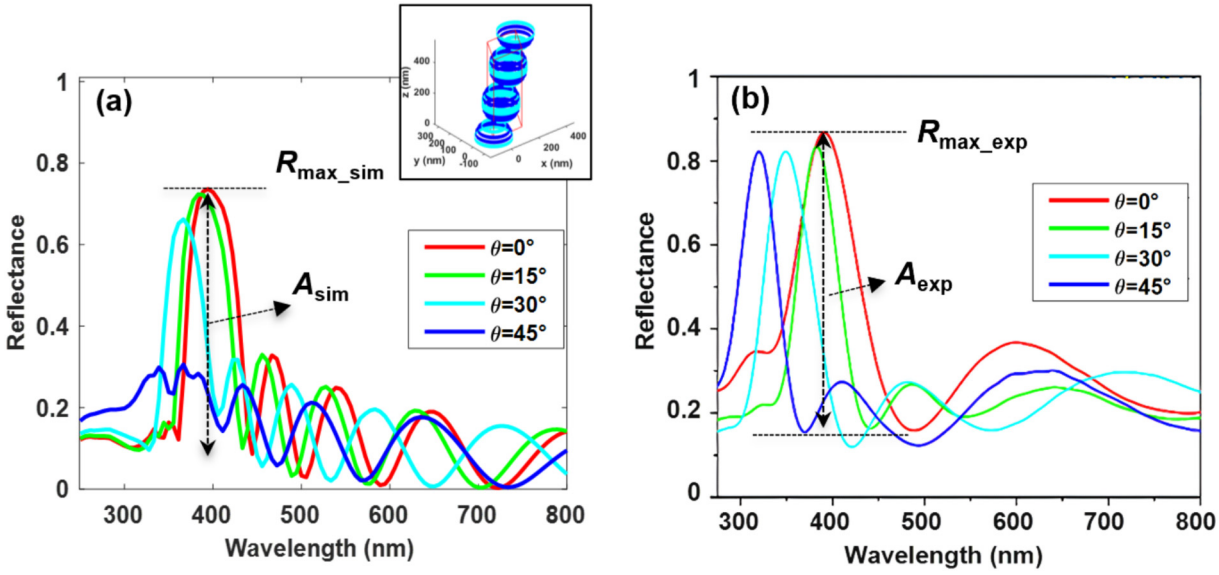

Fig. 1. Reflectance spectrum of ITB-220 slab at different polar angles θ. Simulated spectra (a), measured spectra (reproduced with permission from Ref. [22]. Copyright 2023, Elsevier) (b). Simulation parameters: $N_{uc} = 3$, $N = 61$, $N_g = 81$. For $\theta = 45^{\circ}$, averaging over the azimuth angle φ was performed in the simulation. Inset in (a): a single IO unit cell (for simulations, spheres are discretized into cylindrical layers; those highlighted in cyan are where adjacent spheres interpenetrate due to their dense packing).

films. Based on the wavelength dependence of k of the TiO_2-$BiVO_4$ composite material (Fig. S3, Supplementary Information), the electronic absorption band edge of the TiO_2-$BiVO_4$ composite was estimated to lie in the range 500–600 nm (from the spectral dependence of the extinction coefficient, Fig. S3, Supplmentray Information) in accordance to reported electronic band edge value of 512.4 nm (2.42 eV) [36,37].

2.2. Numerical simulation

The rigorous coupled wave analysis (RCWA) method (see details below) approximates the actual 3D structures by a layered laterally periodic medium [38]. The accuracy of this geometrical representation (Fig. S2, Supplementary Information) improves with the number of layers. For numerical simulations, each unit cell was divided into 61 layers, with each subdivided into 8 identical computational slices. The thickness of each slice was kept below c.a. $\lambda/10$ to ensure good numerical convergence. This layer arrangement was preferred because the reflectance spectra varied substantially for fewer number of layers, while no significant change occurred beyond 61 layers, i.e., numerical convergence was achieved (Fig. S4, Supplementary Information).

The reflectance and absorptance spectra of IO slabs were calculated using the RCWA method [39]. This method is a fully vectorial, three-dimensional, electromagnetic computational technique that is well suited to simulations of the optical response of inverse opals [40,41]. Spectra were calculated at various incident polar angles (θ), assuming a fixed incident azimuthal angle (φ = 0) and non-polarized light. The calculations accounted for contributions of all diffraction orders and evanescent waves [38]. The RCWA relies on the Fourier series expansion of the permittivity in the lateral directions (x and y axis) [38]. The numerical convergence was verified with respect to the number of Fourier coefficients, defined as $N_g = P \times Q$ (where P and Q are the numbers of coefficients along the x and y axis, respectively). Due to inverse opal symmetry, $P = Q$ was chosen. N_g also corresponds to the number of plane waves in the electric and magnetic field expansions [38]. It was determined that $N_g = 9 \times 9$ plane waves were sufficient to obtain satisfactory convergence. Specifically, comparing reflectance spectra for $N_g = 9 \times 9$ and $N_g = 11 \times 11$ revealed that the maximum difference between the two spectra was approximately 5 % of the average spectrum at $\theta = 0^\circ$ and about 2 % at $\theta = 45^\circ$ (Fig. S5, Supplementary Information).

In the RCWA code that we used (TMAT, developed at the University of Namur, Belgium), Fourier expansion of the geometrical features of the layered medium is performed analytically, assuming simple geometrical islands such as cylinders, parallelograms, etc. to describe layers of the IO. When the voids (pores) interpenetrate, cylindrical islands can no more be used to describe the structure. Instead, a mesh of small parallelograms was used to describe the material skeleton (see Fig. S2, Supplementary Information) and the size of the mesh elements was chosen to ensure good convergence.

2.3. Light harvesting enhancement

To fairly evaluate the enhancement of light harvesting in IO slabs due to slow photon effect, a reference slab was required. The choice of this reference must ensure that the same amount of material (TiO_2-$BiVO_4$) is exposed in both the IO slab and the reference slab. Therefore, the latter was defined as an equivalent homogeneous planar slab of thickness (d_{ref}), such that: $d_{ref} = d_{IO} \times f$, where $d_{IO} = N_{uc} \times a_c$ is the IO thickness, $a_c = D\left(\frac{3f}{2\pi}\right)^{-\frac{1}{3}}$ is the lattice constant along (1 1 1) direction, and f the material volume filling fraction.

Based on this reference, the enhancement factor was defined as the ratio of the absorbed photon flux in the inverse opal to that in the reference slab: $EF(\lambda) = \frac{\Phi_{IO}(\lambda)}{\Phi_{ref}(\lambda)}$. The absorbed photon flux (units: $1/(s \times m^2)$) is given by $\Phi(\lambda) = \int \frac{S(\lambda) \cdot A(\lambda)}{E(\lambda)} d\lambda$ [42], where $S(\lambda)$ is the solar irradiance (W m^{-2}), $A(\lambda)$ is the absorptance spectrum, i.e., the fraction of solar irradiance absorbed by the material at a given wavelength, and $E(\lambda) = \frac{hc}{\lambda}$ is the photon energy (J) at a given wavelength λ (h: Planck's constant, c: speed of light).

3. Results and discussion

3.1. Assessment of the inverse opal model

In this section, we first assess the ability of the IO model to represent the optical response of TiO_2-$BiVO_4$ inverse opal samples. For this purpose, we examine the optical response of three TiO_2-$BiVO_4$ inverse opal slabs: ITB-220, ITB-310, and ITB-340. The comparative analysis between simulations and experiments focuses on reflectance spectra, with particular attention to the photonic band gap properties. The simulated reflectance spectra were compared with experimental results obtained by Madanu et al. [22], and the geometrical parameters of the IO slabs were taken from the same reference. To begin, we examined the reflectance spectrum of ITB-220 at various incidence angles (Fig. S6, Supplementary Information). At θ = 0°, θ = 15°, and θ = 30° the simulated spectrum exhibits a single peak which shifts to shorter λ as observed in experiments. However, at θ = 45°, the spectrum no longer exhibits a clear peak. This behavior was highly dependent on the azimuthal angle φ.

For this reason, we averaged the spectrum over azimuthal angles. In reflectance measurements, the exact position of the plane of incidence with respect to the inverse opal geometry is not known, which means that the azimuth angle is random, contrary to the polar angle that is precisely controlled [22]. This justifies the averaging over the azimuth angle in simulations. Since minimal differences were observed at θ = 30° when varying φ, we concluded that azimuthal averaging was unnecessary for θ = 0°, 15°, and 30°. Consequently, azimuthal averaging was performed only at θ = 45° for all slabs (Fig. 1a). Finally, we compared the simulated and experimental optical responses and the PBG properties for the ITB-220 slab, as detailed in Fig. 1, as well as in Fig. S7 and Table S2 (Supplementary Information).

Analysis of the spectra shows that the simulated and measured maximum reflectance values (R_{max}) are in close agreement for all incidence angles. Although deviations exist, the absolute differences are lower than 0.16, up to θ = 30°. This suggests that the theoretical model reproduces quite well the level of reflectance. The larger discrepancy observed at 45° probably originates from structural imperfections of the IO sample, which do not enable to reproduce fine details of the spectra at oblique incidence, as expected for a perfect IO structure. For $\theta = 0^\circ$, 15°, and 30°, both simulated and experimental values of the peak amplitude A, i.e., distance between the top and the bottom of the peak, see Fig. 1, are relatively close, with absolute differences not exceeding 0.05 up to $\theta = 30^\circ$. More importantly, the simulated and measured peak positions (λ_{peak}) are well aligned for all angles. At low angles (0° and 15°), deviations are particularly small (~4–5 nm), indicating that the theoretical model effectively captures the angular dependence of the reflectance peak position. However, a larger deviation (18 nm) is observed at 45°, which again may be attributed to increased scattering at oblique incidence, sample's structural imperfections, and experimental limitations in reflectance measurement at more grazing angles. The full width at half maximum (FWHM) values

also exhibit good agreement between theory and experiment, though with some discrepancies, particularly at 15° and 45°. These discrepancies may again arise from structural imperfections. Overall, the simulated and measured reflectance properties are highly consistent, especially at polar angles not too far from normal incidence. This agreement validates the reliability of the theoretical model in predicting the optical response of the TiO_2-$BiVO_4$ inverse opal structure. The same conclusion was reached when comparing the simulated and measured reflectance spectra of ITB-310 and ITB-340 slabs (see Figs. S8, S9, and S10, Tables S3 and S4, Supplementary Information). For both slabs, the simulated peak wavelength matches well the measured peak wavelength, with deviation lower than 16 nm. For ITB-310, the theoretical FWHM is slightly larger than the experimental value, whereas for ITB-340, it is consistently smaller. The simulated (A_{sim}) and experimental (A_{exp}) peak amplitude values show good agreement for both ITB 310 and ITB 340 slabs, as the absolute differences ($|\Delta A|$) remain small. The deviations are within reasonable margins, not exceeding 0.22, and fall within expected experimental uncertainties, indicating that the theoretical model accurately captures the experimental trends.

3.2. Prediction of the absorbed photon flux

Photocatalysis can occur in both gaseous and liquid media. In photonic crystals, the slow photon effect is stronger when the refractive index contrast is higher, leading to enhanced light-matter interactions. Experimentally, this corresponds to gas-phase photocatalysis, where the incident medium is air ($n_{inc} = 1.0$), and the pores of the inverse opal structure are filled with air ($n_{pore} = 1.0$). In liquid-phase photocatalysis, the pores become filled with water ($n_{pore} = 1.33$), as analytes such as rhodamine B are typically dissolved in aqueous solutions, which reduces the refractive index contrast between the pores and the skeleton. Additionally, the incident medium is also water ($n_{inc} = 1.33$). As a result, the slow photon effect weakens, leading to a lower overall enhancement factor. By first simulating the IO system in air, we captured the strongest photonic effects before evaluating how they are modified in water.

3.2.1. Absorption enhancement at normal incidence

The added value of simulations is their ability to predict the absorptance, a quantity of interest which evaluates the light harvesting potential for photocatalysis but is challenging to measure in practice. To compare the performances of TiO_2-$BiVO_4$ inverse opal (ITB) slabs with those of reference TiO_2-$BiVO_4$ thin films (TB), in terms of absorbed photon fluxes, we calculated reflectance and absorptance spectra of each of them at normal incidence, with air as both incidence medium and pore medium (Fig. 2 shows the case of ITB-220). The purpose of calculating the reflectance spectrum was to enable the identification of the photonic band gap edges (vertical dashed lines in Fig. 2). For a fair comparison, it is essential to ensure that the same amount of TiO_2-$BiVO_4$ is present in both ITB and TB models. As already explained (Materials and Methods), this equivalence can be achieved by choosing the thickness of TB model such that: $d_{film} = d_{IO} \times f_{TiO_2-BiVO_4}$ where d_{film}, d_{IO} and $f_{TiO_2-BiVO_4}$ are respectively the thickness of the thin film, the thickness of the IO slab and the volume filling fraction of TiO_2-$BiVO_4$ in the IO slab.

The reflectance of ITB-220 (Fig. 2a) shows a pronounced PBG peak with blue edge (BE) and red edge (RE) easily identified on both sides, respectively at λ_{BE} = 361 nm and λ_{RE} = 444 nm. The reference TB exhibits a lower reflectance with typical thin film oscillations. Around the BE, light trapping occurs due to the slow photon effect, which leads to enhanced light-material interaction in both TiO_2 skeleton and $BiVO_4$ particles attached to it, since both materials absorb in the region. The RE is also associated with the slow photon effect, but the enhanced interaction concerns $BiVO_4$ only since it absorbs visible light whereas TiO_2 absorption is limited to UV light. The thin film (TB) lacks the PBG and thus has lower optical performance in these regions. These considerations are supported by the absorptance spectra (Fig. 2b). The simulation results show that the absorptance of ITB-220 is higher than that of the equivalent homogeneous film TB in the different regions of the spectrum. In fact, in the region where the intrinsic absorption of both TiO_2 and $BiVO_4$ is high (λ < 350 nm) (see Fig. S3 supplementary information), light is efficiently absorbed before it can significantly interact with the photonic structure. As a result, slow photon effects cannot develop because light does not penetrate deep enough to experience PBG edge enhancements.

Moreover, ITB-220 exhibits higher absorptance than the planar reference of the same volume of material due to the anti-reflection effect that is provided by the pores shown on the surface, which form an index-matching corrugation. Thanks to their surface corrugation, the incident light penetrates more efficiently in the IO than in the reference slab with a flat surface. In the region where the intrinsic absorption of TiO_2 is small, i.e. around 350 nm (near the electronic band edge of TiO_2), resonantly enhanced absorption can occur due to the slow photon effect, if one of the PBG edges is properly tuned to this wavelength [24]. This is the case observed here (Fig. 2b), where a small peak shows up on top on the absorptance spectrum of ITB-220, which is absent in the TB slab. This peak is due to the BE of the PBG that is tuned to this wavelength.

The slow photon effect could enhance the absorptance in $BiVO_4$ but it is less significant since $BiVO_4$ exhibits strong intrinsic absorption at 350 nm. Indeed, photons at 350 nm hardly penetrate in $BiVO_4$ particles that are deeper in the IO structure. The absence of this peak at 350 nm in TB confirms that the enhancement originates from the structural properties of ITB-220 rather than intrinsic material absorption. Between 350 and 450 nm, a dip is observed in the absorptance of ITB-220. This reduced absorption is caused by the PBG and is responsible for lower light harvesting in this region, compared with the TB thin film.

In the region where only $BiVO_4$ has intrinsic absorption (350–550 nm), the slow photon effect can also enhance the absorptance. This is the case around 450 nm, where the strong peak is due to the RE of the PBG that is tuned around this wavelength. This extended absorption into the visible range is essential for efficient photocatalysis using solar light. In contrast, the TB thin film again lacks this photonic enhancement, resulting in comparatively weaker absorptance. Finally, two other absorptance enhancement peaks are observed at 500 and 578 nm above the RE of the PBG. They correspond to minima in the reflectance spectrum (Fig. 2a). These minima are likely associated with Fabry-Perot interference across the slab thickness. At these wavelengths, light is trapped in the cavity formed by the front and rear interfaces, forming standing waves. The multiple passage of light due to reflections at both interfaces increases its interaction with the materials, hence the absorptance. This effect can be interpreted as a coherent scattering effect in the effective Bragg reflector to which, near normal incidence, the IO structure can be assimilated [19]. The predicted absorption enhancement at normal incidence in ITB-220 will turn into enhanced photocatalytic efficiency (see section 3.2.4), which is beneficial for sterilization, air and water disinfection applications (see section 3.2.3).

3.2.2. Effect of the angle of incidence

In real photocatalytic applications, the angle of incidence of solar light varies due to the position of the sun in the sky. In photocatalytic activity tests, the orientation of the photonic crystals in the reactor determines light incidence conditions. To investigate

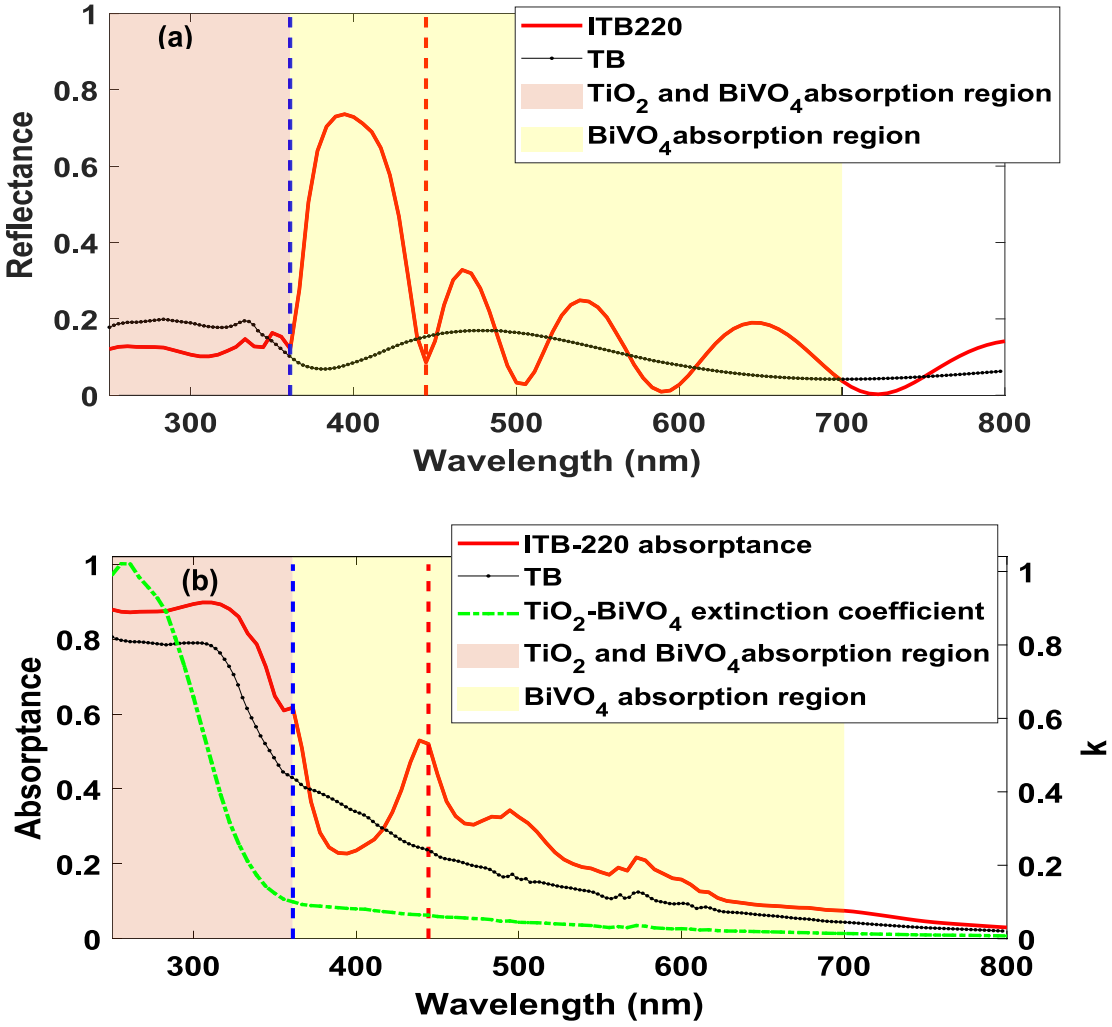

Fig. 2. Reflectance (a) and absorptance (b) spectra of ITB-220 slab and reference TB thin film at normal incidence ($\theta = 0^{\circ}$). The incidence medium and pore medium is air. The dashed vertical lines indicate the position of the PBG edges (blue and red edges). Simulation parameters: $N_{uc} = 3$, $N = 61$, $N_g = 81$.

the impact of the incidence angle on the optical response of the photocatalyst, we calculated reflectance and absorptance spectra of ITB-220 slab at different angles (0°, 15°, 30°, and 45°) (Fig. 3). These values were selected to match angles used in reflectance measurements reported in [22], enabling direct comparison between our simulations and experimental data. The spectra provide insights into how the photonic bandgap and slow photon effects evolve with the angle, highlighting shifts in resonance conditions and variations in absorption efficiency.

At short wavelengths (λ < 350 nm), the absorptance of ITB-220 remains almost unchanged up to $\theta = 30^{\circ}$ and is still higher than the TB absorptance at all incident angles. This is because, in this region, the intrinsic absorption of both TiO_2 and $BiVO_4$ is strong, meaning that light is absorbed before it can interact significantly with the photonic structure. In this case, the IO structure does not play a significant role in modifying the absorptance at different angles in this region. At every angle, the IO slab absorbs light more efficiently than the TB thin film due to its antireflective surface corrugation as already mentioned above. Near the TiO_2 electronic band edge (λ≈350 nm), the small peak attributed to the BE of the PBG shifts to shorter wavelengths and weakens as the incident angle increases. This shift results from the angle-dependent modification of the PBG, where a larger angle effectively reduces the periodicity of the inverse opal structure, shifting the PBG to shorter wavelengths [19]. The shift of the PBG is also evident when observing the brood absorptance dip associated with the strong PGB reflection of the IO (around 400 nm at normal incidence). The weakening of the peak suggests that the slow photon effect is the strongest at normal incidence and becomes less effective at larger angles, as the interaction between the incident light and the photonic structure diminishes, thereby reducing the absorptance enhancement. A similar behavior is observed in the $BiVO_4$-related absorption region (400–500 nm), where the absorptance remains strong at different angles. The resonant peak around 450 nm, due to the RE of the PBG, also shifts towards shorter wavelengths as the angle increases. This shift is explained in the same way as before: an increase of the incidence angle reduces the effective periodicity of the IO structure, shifting the RE to shorter wavelengths [19]. The simulations confirm that the inverse opal periodic structure plays a crucial role in modulating the absorptance behavior of both TiO_2 and $BiVO_4$, beyond their intrinsic material properties. Two other absorptance enhancement peaks are observed at 500 nm and 578 nm, which correspond to minima in the reflectance spectrum. These minima are associated with Fabry-Perot interference across the slab thickness. As previously explained, these peaks are due to the finite thickness of the IO slab. These results clearly demonstrate that the inverse opal structure significantly enhances light absorptance across a wide range of wavelengths and incident

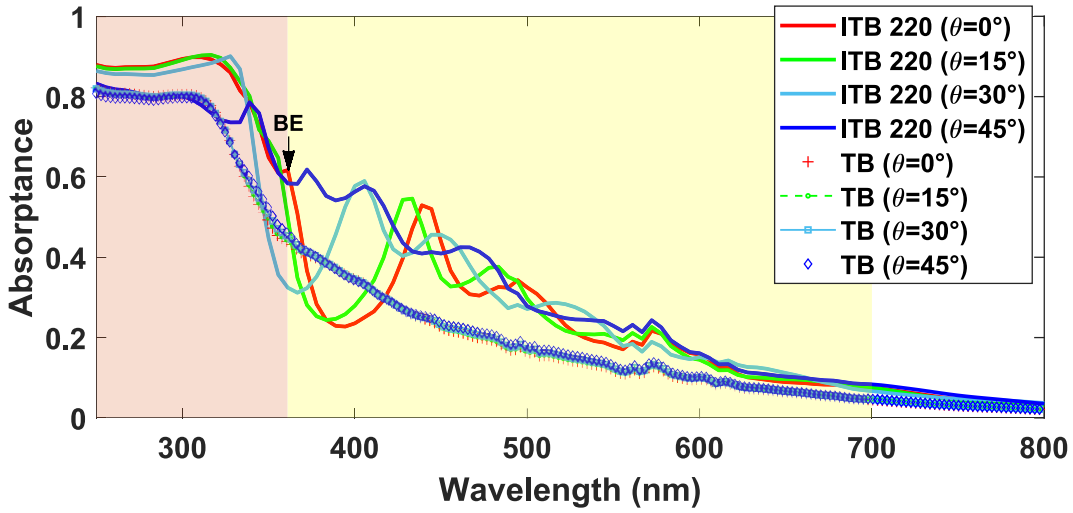

Fig. 3. Absorptance spectra of ITB-220 and TB slabs at different incidence angles θ. TB is the reference thin film. The incidence medium and pore medium is air. The small arrow labeled BE indicates the blue edge of the PBG for ITB-220 at θ = 0°. The shaded regions represent the common absorption region of TiO_2 and $BiVO_4$ (pink) and the absorption region of $BiVO_4$ only (yellow).

angles, not only through the intrinsic absorption of TiO_2 and $BiVO_4$, but also through photonic effects—such as photonic bandgap formation, slow photon enhancement, Fabry-Perot interference, and antireflective surface corrugation that intensify light-matter interactions. As shown in Fig. 3, the absorption enhancement in ITB-220 is maintained over a large range of incidence angles. This angular robustness is found in photocatalytic efficiency as well (see Section 3.2.4), which is beneficial for applications of this IO structure.

3.2.3. Influence of the pore diameter

In this section, we investigate the influence of pore diameter on the optical properties of the ITB structure under both normal and oblique incidences. By analyzing how changes in pore size affect reflectance, absorptance, and PBG behavior, we aim to better understand the role of structural parameters in tuning the optical response of the inverse opal.

Reflectance and absorptance spectra were calculated for different pore diameters (ITB-220, ITB-310, and ITB-340), at normal incidence (Fig. 4). As the pore diameter increases, the PBG shifts toward longer wavelengths, as expected [19,22]. Interestingly, for ITB-310 and ITB-340, a second order PBG appears around 230 and 300 nm, respectively. The appearance of the second order Bragg peak was confirmed by analyzing the reflectance spectra without absorption, i.e., by setting the extinction coefficient (k) to zero (Fig. S11, Supplementary Information). This analysis allowed us to locate the edges of the 2nd order PBG (dotted vertical lines in Fig. 4 for the RE). Indeed, in the presence of absorption, it is difficult to estimate the peak wavelength of the 2nd order PBG from either reflectance or absorptance spectra (Fig. 4). At the red edges of the second order PBG (350.0 and 377.7 nm), enhanced absorption occurs due to the slow photon effect. Similarly, it takes place at both the blue and red edges of the first PBG, increasing absorptance in these regions (Fig. 4b). The exploitation of higher-order PBG for slow photons was already pointed out in [43]. Our study shows an example of such a strategy based on models of real samples.

The studied inverse opal structures with varying pore diameters exhibit distinct advantages for photocatalytic applications (Fig. 4b). The IO structure with the small pore diameter (ITB-220) exhibits strong absorption in the 250–330 nm range, covering both UV-C and UV-B regions. UV-C light (200–280 nm) is well known for its germicidal properties, as it can effectively destroy the DNA and RNA of microorganisms, including bacteria, viruses, and fungi, rendering them inactive [44].

When the photocatalyst absorbs UV light within this range, it generates reactive oxygen species (ROS), which enhance its ability to kill pathogens in air, water, and on surfaces [45]. This makes photocatalysts such as ITB-220 (with the smallest pore size) an excellent candidate for sterilization and disinfection applications [46].

Additionally, it facilitates the photocatalytic degradation of volatile organic compounds (VOC) and other air pollutants. The ROS generated upon UV absorption break down organic pollutants into less harmful substances, such as CO_2 and H_2O [47]. The slow photon effect further enhances light harvesting, thereby boosting pollutant degradation and rendering it effective for air purification [48].

The IO structure with the intermediate pore diameter (ITB-310) exhibits strong absorptance in both UV-A (333–400 nm) and visible spectrum (400–700 nm). Its dual PBG, i.e., first and second PBGs, facilitates the generation of ROS [49], under low-intensity, broad-spectrum indoor lighting (e.g., LEDs, fluorescent lamps). The slow photon effect near the photonic band edges enhances light-matter interaction, increasing ROS production and facilitating the continuous degradation of indoor VOCs (e.g., toluene, benzene) [48]. This makes a photocatalysts such as ITB-310 an effective photocatalyst for indoor air remediation [48].

In contrast, the IO structure with the large pore diameter (ITB-340) also demonstrates high absorption in the UV-A region but has superior absorption in the visible light range, particularly between 400–550 nm. This enhanced light harvesting, due to dual PBG and related slow photon effects, makes this structure highly effective for solar-light-driven photocatalysis [25]. These properties are advantageous in outdoor environments, where natural sunlight can be utilized to efficiently oxidize airborne pollutants such as NO_x, SO_x, and low-concentration VOCs [50,51]. This makes photocatalysts such as ITB-340 promising for outdoor air remediation applications [51]. Overall, our findings highlight the tunability of optical properties through sphere size tuning, which can be leveraged to optimize photocatalytic performance across specific spectral regions.

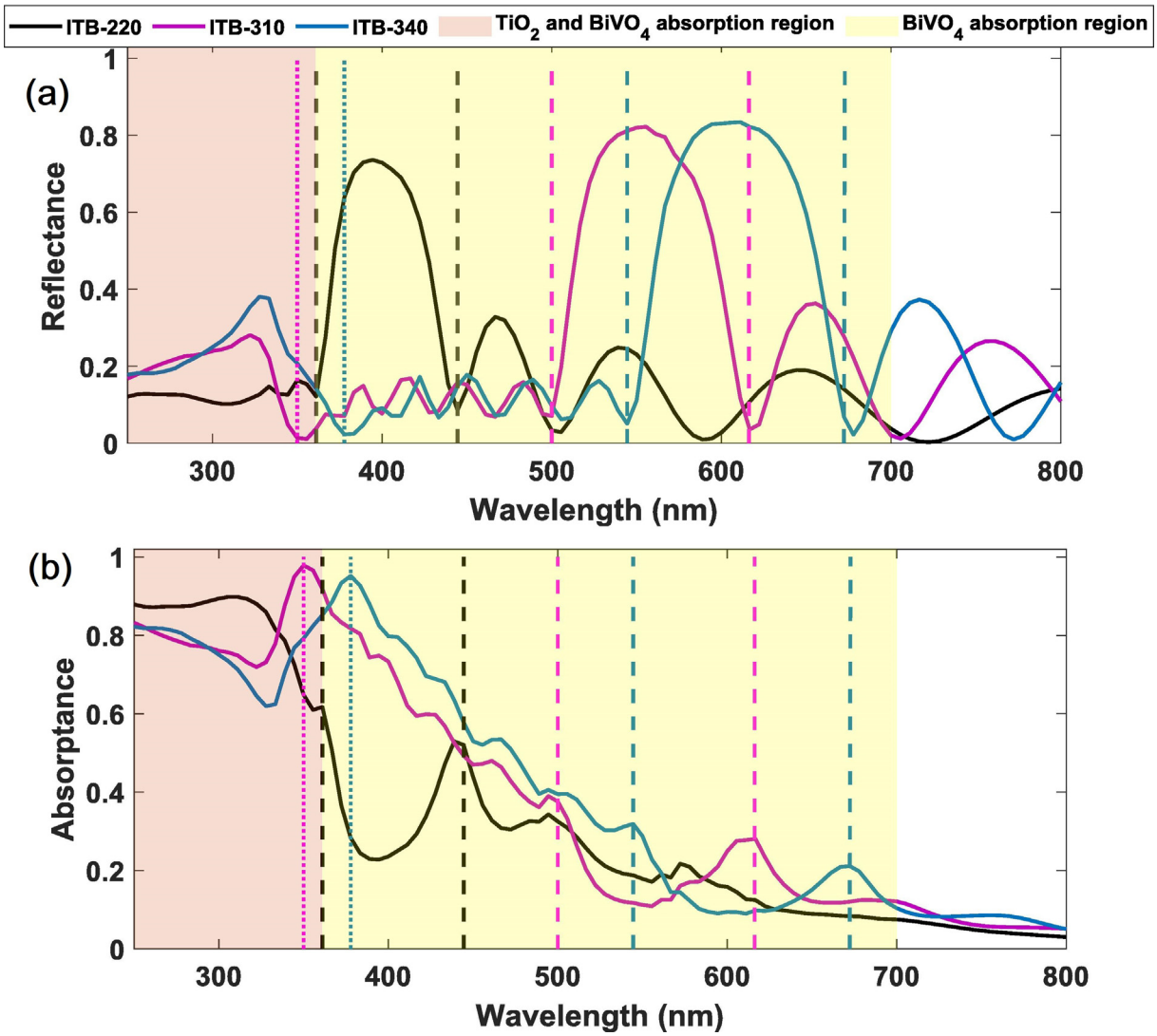

Fig. 4. Reflectance (a) and absorptance spectra (b), of ITB-220, ITB-310, and ITB-340 slabs at normal incidence in air. The vertical dashed lines indicate the position of the BE and RE of the 1st order PBG. The vertical dotted lines indicate the RE of the 2nd order PBG.

The original IO structures were optimized for high harvesting at normal incidence [22]. We also investigated the influence of the pore diameter on absorptance spectra at oblique incidence (15°, 30°, and 45°) for the three models (Fig. 5). At oblique incidence, the absorptance spectra of those structures exhibit noticeable angular dependence due to the interplay between intrinsic material absorption and photonic effects. In the UV region (λ < 400 nm), where both TiO_2 and $BiVO_4$ absorb strongly, the absorptance remains relatively stable when the incident angle varies, confirming that intrinsic absorption dominates in this spectral range. However, in the UV-A region (315–400 nm), the intermediate-pore and large-pore structures show a slight shift of their second PBG edges towards shorter wavelengths as the incident angle increases, a direct consequence of the reduced effective periodicity of the inverse opal structure. This shift weakens the slow photon effect, due to a detuning from ideal band edges positions, while it leads to a gradual decrease in absorptance enhancement. In the visible range (400–550 nm), a similar trend is observed, particularly around 450 nm, where the RE of the 1st order PBG in the small-pore structure also blue shifts, leading to detuning from optimal position. Despite the angular shift, the intermediate and large-pore structures maintain strong absorptance in this region, demonstrating their robustness for photocatalytic applications under visible light. In contrast, the small-pore structure, which lacks a second order PBG, experiences a more pronounced reduction in absorptance at oblique incidence, indicating a greater sensitivity to angular variations. Overall, these results demonstrate that, while slow effects are pronounced at normal incidence because original structure parameters were optimized accordingly [22], they persist at oblique angles, particularly in the intermediate-pore and large-pore inverse opals, making these structures more effective for photocatalytic applications under real-world solar illumination. The impact of predicted absorption enhancement in IO structures with different sphere diameters on specific applications is justified hereafter by the evaluation of photocatalytic performance (see next section 3.2.4).

3.2.4. Photocatalytic efficiency

To further evaluate the impact of the photonic structure on light absorption and photocatalytic performance, we now compare the absorbed photon flux enhancement factors of the three models under different incidence angles. The goal of this comparison is to identify the highest absorbed photon flux enhancement achievable among the three models and to correlate it with the

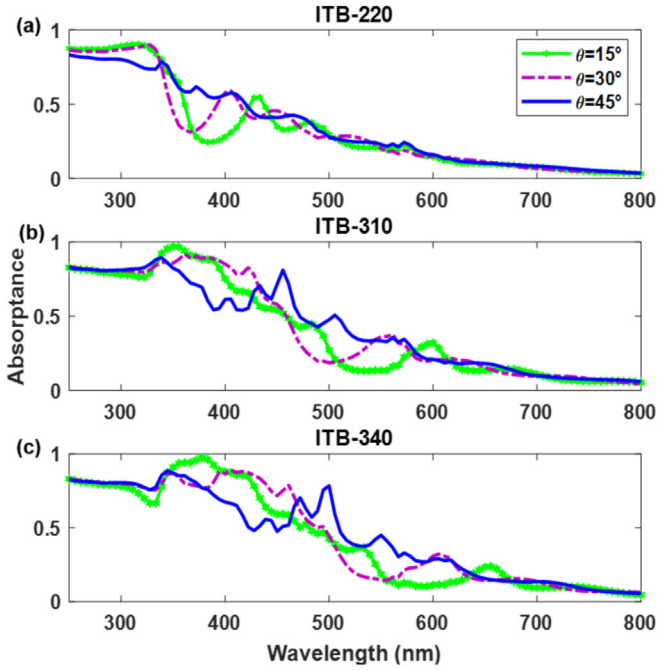

Fig. 5. Absorptance spectra (in air) for the small-pore (a), intermediate-pore (b), and large-pore (c) IOs at oblique incidence.

best photocatalytic efficiency measured in corresponding ITB samples [22] at different angles (Fig. 6). The enhancement factor, i.e., the ratio between the absorbed photon flux in ITB models to that in the corresponding reference slabs, quantifies how much light is more efficiently captured by the photonic structures. The values of the absorbed photon flux for ITB and reference slabs are reported in Fig. S12 (Supplementary Information). All ITB structures investigated here exhibit enhancement factors greater than unity (1.4 to 1.7), confirming that these inverse opal structures enhance light absorption compared to the reference slab. The enhancement factor increases with the incidence angle, indicating that multiple scattering and extended optical path lengths improve light-trapping efficiency under oblique illumination. Although absorptance spectra change markedly at higher angles (Fig. 5), the studied inverse opal structures still outperform the reference slab in terms of overall photon flux enhancement.

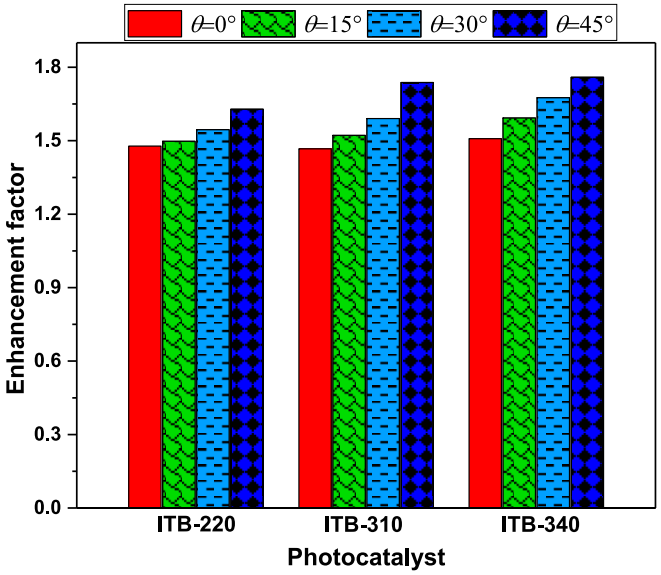

Fig. 6. Enhancement factors (Φ_{IO}/Φ_{ref}) of the absorbed photon flux Φ for the small-pore, intermediate-pore, and large-pore IOs at different incidence angles.

Among the three structures, ITB-220 shows the lowest enhancement factor (1.47 at normal incidence), due to its limited visible light response, leading to weaker absorbed photon flux. ITB-310 exhibits a slightly higher enhancement factor than ITB-220, especially at 30° and 45°, thanks to enhanced visible light absorption and cumulated photonic band edge effects. ITB-340 demonstrates the highest enhancement factor, particularly at 30° and 45°, making it the most efficient photocatalyst model for capturing light and the best candidate for solar light-driven photocatalysis. The continuous increase of the enhancement factor at larger angles suggests that photon-matter interaction within the periodic structure is better utilized under tilted light incidence, reinforcing the advantages of the inverse opal design.

3.2.5. Influence of the slab thickness

In the previous sections, all analyses were conducted using ITB slabs with a fixed thickness of three IO unit cells. Since ITB-340 exhibited the highest performance among the three models, we also investigated how its optical response, specifically absorptance and photon flux, evolves with the slab thickness at normal incidence (Fig. 7). Absorptance spectra were calculated (Fig. S13, Supplementary Information) by varying the number of unit cells ($N_{uc} \in [2,6]$), where each unit cell corresponds to a vertical stack of three spheres in the inverse opal lattice. It was checked that the slab thickness scales linearly with the number of spheres in the IO (Fig. S14, Supplementary Information).

Increasing the number of unit cells enhances the absorptance at the RE (Fig. 7b) of both the 1st and 2nd order PBGs. Notably, the absorptance at the 2nd order PBG (~380 nm, UV range) remains at a nearly fixed wavelength (377 nm) for all thicknesses and reaches near-unity value (for $N_{uc} \geq 3$), highlighting efficient photon confinement in relatively thin structures. In the visible range, the absorptance at the 1st order PBG gradually shifts toward shorter wavelengths as the number of unit cells increases and it increases more gradually, reflecting enhanced light trapping as the structure becomes thicker.

This absorption enhancement is further supported by the photon flux analysis (Fig. 7a), which exhibits a saturation trend: although the photon flux increases with thickness, the gain becomes less significant beyond $N_{uc} = 3$. For three-unit cells (thickness ~2178 nm), the photon flux already reaches 4.45×10^{20} ($s^{-1}\,m^{-2}$), which corresponds to more than 70 % of the maximum value obtained for six-unit cells. This saturation behavior indicates that most of the incident photons are already being absorbed before reaching the bottom of the slab. Further increases in thickness contribute less to the enhancement due to reflection, interference, and intrinsic material losses. Overall, a slab of three IO unit cells emerges as an optimal configuration, offering a balance between strong photonic enhancement, efficient absorption, and practical film thickness for fabrication.

3.3. Pores filled with water

In liquid-phase photocatalysis, the incident medium is a water solution (n_{inc} = 1.33) containing the analyte, and the porous network is infiltrated with that solution (n_{pores} = 1.33). In practice, diluting aqueous analyte solutions used in photocatalytic experiments (e.g., 1.5 μM RhB solution in [22]) have refractive indices close to that of pure water and are therefore expected to have negligible impact on light propagation. Nevertheless, more concentrated solutions could induce optical absorption at specific wavelengths, influencing light propagation in the IO structure. In

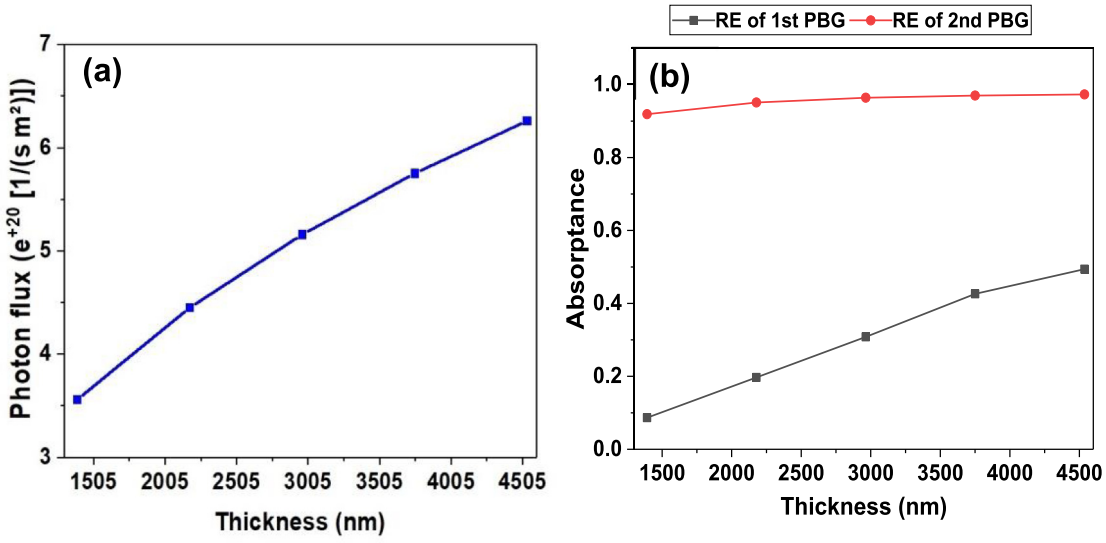

Fig. 7. Absorbed photon flux (a) and absorptance (b) at RE wavelengths as a function of the IO slab thickness for ITB-340.

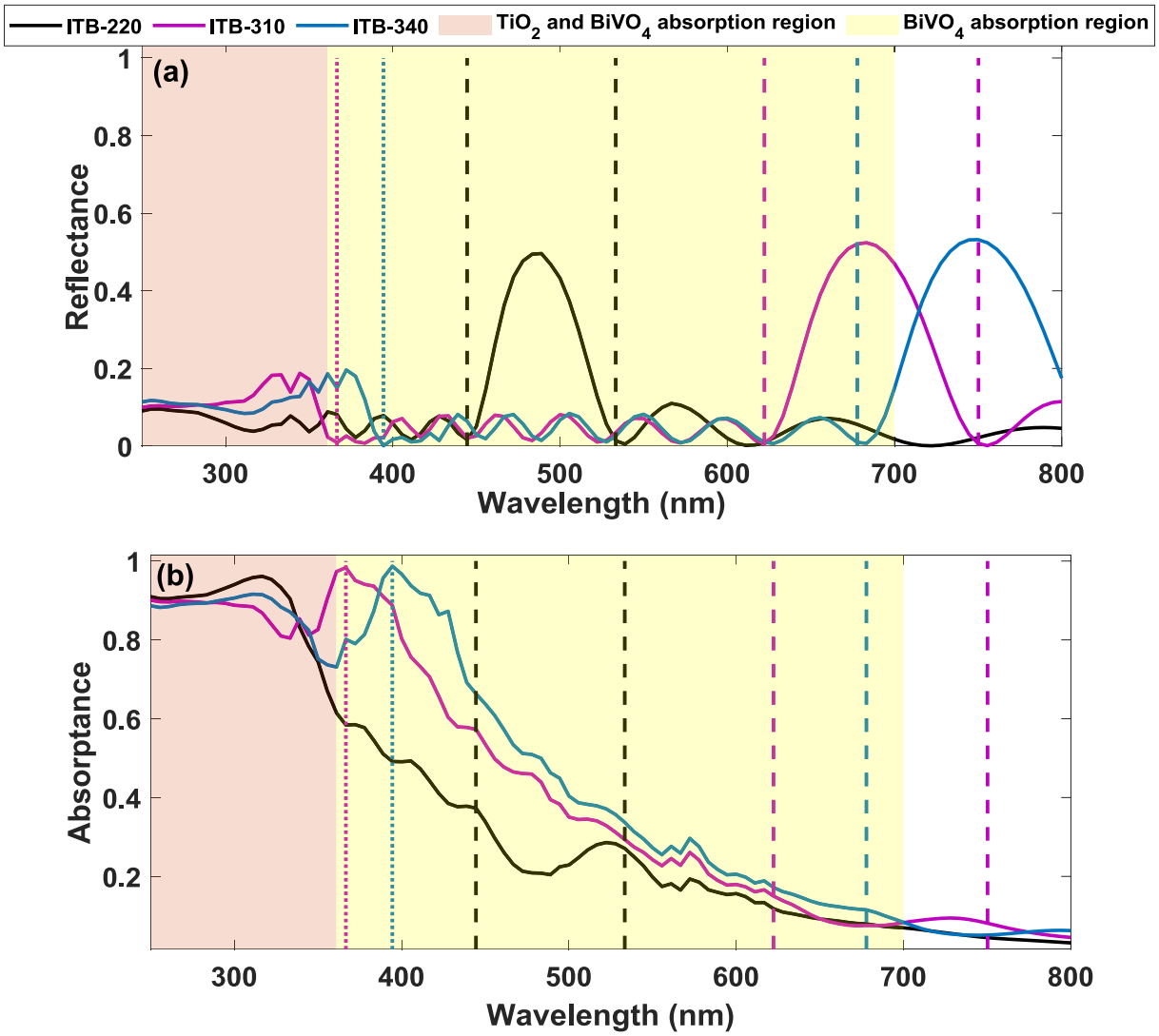

Fig. 8. Reflectance (a) and absorptance (b) spectra for ITB-220, ITB-310, and ITB-340 slabs at normal incidence in water. The vertical dashed lines indicate the positions of the BE and RE of the 1st order PBG. The vertical dotted lines indicate the RE of the 2nd order PBG.

these cases, more realistic simulations could be done using an effective complex refractive index for the pore filing medium, which is straightforward in our RCWA code.

The reflectance and absorptance spectra as well as the enhancement factor were calculated for the three ITB structures at both normal and oblique incidences accordingly. The reflectance and absorptance spectra (Fig. 8) shift to longer wavelengths due to the reduced refractive index contrast between the IO structure and its surroundings.

However, photonic effects remain prominent. Even in the water phase, all ITB structures exhibit absorptance higher than the TB absorptance at all incident angles (Fig. S15, Supplementary Information), and thus photon flux enhancement factors are greater than unity (Fig. 9), confirming their ability to outperform the reference slab in terms of light absorption. This indicates that the inverse opal architectures retain effective light-trapping capabilities despite the lower refractive index contrast in water. Although the overall enhancement is slightly reduced compared to the air phase, primarily due to the higher optical density of water, the consistent increase in photon flux with increasing incident angle underscores the robustness and efficiency of these nanostructures. The predicted absorbed photon fluxes (Fig. S12) can be compared with photocatalytic RhB degradation efficiency data reported in [22] (Fig. 6). Trends in simulation and experimental data agree, confirming the superior performance of ITBs (samples and models) with respect to reference slabs.

The IO structure with the small pore diameter exhibits significant absorptance in the UV-C and UV-B regions, like in the air phase. The produced ROS can effectively inactivate bacteria and viruses by damaging their cellular components, making this structure ideal for water disinfection and pathogen inactivation [52]. Furthermore, the efficient UV absorption boosts photocatalytic activity, enabling the breakdown of persistent organic pollutants, including pharmaceutical residues and emerging contaminants, positioning this structure as a promising candidate for wastewater treatment [53]. The IO structure with the intermediate pore diameter demonstrates strong absorptance in both the UV-A (333–400 nm) and the visible spectrum (400–550 nm) due to its dual PBG. This makes it effective for water purification and pollutant degradation [54]. The dual PBG also makes photocatalysts such as ITB-310 effective for degrading organic contaminants and dyes [55]. Previous studies have demonstrated the effectiveness of TiO_2-$BiVO_4$ composites in degrading organic pollutants, reinforcing its suitability for water treatment applications [12,56]. The IO structure with the largest pore diameter has superior absorption in the visible range, making it highly effective for visible-light-driven photocatalysis. The presence of dual PBG and slow photon effects further improve light harvesting, as noticed before. This structure is well-suited for environmental and energy applications, such as hydrogen production and organic pollutant degradation.

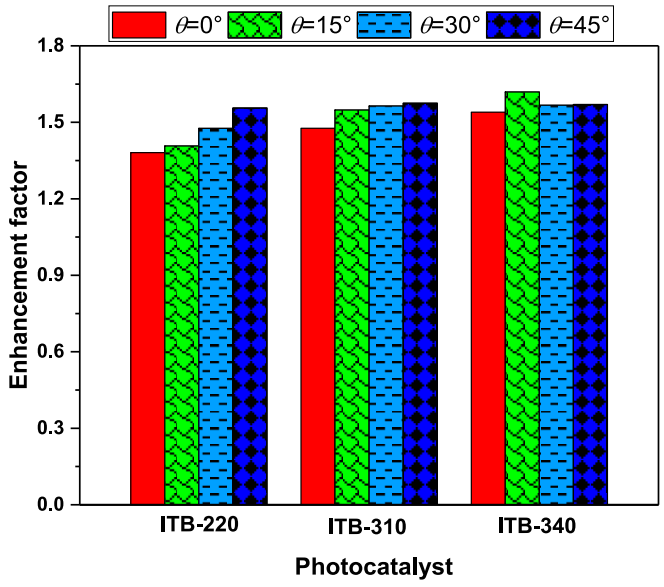

Fig. 9. Enhancement factors of the absorbed photon flux for the small-pore, intermediate-pore, and large-pore IOs at different incidence angles, in water.

Building on previous studies demonstrating the visible-light-driven hydrogen evolution capabilities of TiO_2-$BiVO_4$ composites [57,58], ITB-340 offers compelling potential for efficient solar hydrogen production.

4. Conclusions

We presented a detailed computational analysis of light harvesting properties and photocatalytic potential of TiO_2-$BiVO_4$ inverse opal structures, in air and in aqueous medium, at varying incidence angles. The theoretical IO model was proven to be consistent with previously reported experimental results. Among investigated structures, the small-pore IO exhibited strong absorption in UV-C and UV-B regions but showed limited visible-light response, making it better suited for UV-driven applications such as sterilization, air and water disinfection. The medium-pore IO demonstrated a balanced absorption between UV and visible regions, benefiting from slow photon effects at the edges of the 1st and 2nd order PBGs (dual photonic band edge enhancement), making it an excellent candidate for photocatalysis under both UV and visible light, particularly for indoor air remediation and water purification, including the degradation of organic pollutants. The large-pore IO, which exhibited the highest photon flux enhancement, particularly at oblique angles, proved to be the most efficient for solar-driven photocatalysis. Its excellent performance under visible light highlights its potential for applications such as outdoor air remediation, hydrogen production and environmental remediation of water. All IO structures outperformed the planar reference slabs in terms of overall photon flux enhancement, emphasizing the role of slow photon effects in improving light-matter interactions. We believe these findings will contribute to more efficient optimization of inverse opals for sustainable energy and environmental applications. Still, some issues must be acknowledged in practice. Defects in the periodic structure may affect the slow photon effect, hence the efficiency of light harvesting enhancement. Though already good photocatalytic performances were obtained on TiO_2-$BiVO_4$ IOs presenting some defects (such as cracks), it would be interesting to account for the presence of defects in optical simulations. This is entirely possible with RCWA using a super-cell approach [59] in which the IO unit cell is extended to accommodate for defects. The size of the super-cell will set the computation burden for a desired accuracy. Large-scale fabrication of IO structures remains challenging, especially for controlling pore geometry and defect level. For composite IOs, the control of the heterojunction is an additional challenge for charge transfer.

CRediT authorship contribution statement

Oumayma Habli: Writing – review & editing, Writing – original draft, Validation, Methodology, Investigation. **Thomas L. Madanu:** . **Bao-Lian Su:** Writing – review & editing, Visualization, Validation. **Olivier Deparis:** Writing – review & editing, Validation, Supervision, Methodology, Investigation.

Declaration of competing interest

The authors declare that they have no known competing financial interests or personal relationships that could have appeared to influence the work reported in this paper.

Acknowledgments

This research used resources of the "Plateforme Technologique de Calcul Intensif (PTCI)" (http://www.ptci.unamur.be) located at the University of Namur, Belgium, which is supported by the FNRS-FRFC, the Walloon Region, and the University of Namur (Conventions No. 2.5020.11, GEQ U.G006.15, 1610468, RW/GEQ2016 et U.G011.22). The PTCI is member of the "Consortium des Équipements de Calcul Intensif (CÉCI)" (http://www.ceci-hpc.be).

This project has received funding from the European Union's Horizon 2020 research and innovation program under the Marie Sklodowska Curie grant agreement n°101034383.

Appendix A. Supplementary material

Supplementary data to this article can be found online at https://doi.org/10.1016/j.jechem.2025.09.035.

References

[1] T. Su, X. Zhu, Materials 16 (2023) 7197.
[2] V. Van Pham, W.-J. Ong, Beilstein-Institut. 14 (2023) 722–724.
[3] M. Nasr, C. Eid, R. Habchi, P. Miele, M. Bechelany, ChemSusChem 11 (2018) 3023–3047.
[4] M.-A. Gatou, A. Syrrakou, N. Lagopati, E.A. Pavlatou, Reactions 5 (2024) 135–194.
[5] N. Ramesh, C.W. Lai, M.R.B. Johan, S.M. Mousavi, I.A. Badruddin, A. Kumar, G. Sharma, F. Gapsari, Heliyon 10 (2024) e40998.
[6] B. Bakbolat, C. Daulbayev, F. Sultanov, R. Beissenov, A. Umirzakov, A. Mereke, A. Bekbaev, I. Chuprakov, Nanomaterials 10 (2020) 1790.
[7] H. Dong, G. Zeng, L. Tang, C. Fan, C. Zhang, X. He, Y. He, Water Res. 79 (2015) 128–146.
[8] X. Zhou, J. Liang, L. Xu, S. Wu, M. Xie, Q. Liang, J. Luo, X. Fan, X. Zhou, J. Colloid Interface Sci. 689 (2025) 137240.
[9] P. Akhter, A. Arshad, A. Saleem, M. Hussain, Catalysts 12 (2022) 1331.
[10] S. Bingham, W.A. Daoud, J. Mater. Chem. 21 (2011) 2041–2050.
[11] M. Zalfani, B. Van Der Schueren, Z.-Y. Hu, J.C. Rooke, R. Bourguiga, M. Wu, Y. Li, G. Van Tendeloo, B.-L. Su, J. Mater. Chem. A 3 (2015) 21244–21256.
[12] Y.-R. Lv, C.-J. Liu, R.-K. He, X. Li, Y.-H. Xu, Mater. Res. Bull. 117 (2019) 35–40.
[13] K.R. Tolod, S. Hernández, N. Russo, Catalysts 7 (2017) 13.
[14] Y. Chen, X. Li, H. Yang, Y. Huang, Small 20 (2024) 2402406.
[15] L. Xu, Y. Zhang, B. Liu, K. Wan, X. Wang, T. Wang, L. Wang, S. Wang, W. Huang, ACS Nano 19 (2025) 15863–15875.
[16] S. Wang, K. Wan, J. Feng, Y. Yang, S. Wang, J. Mater. Sci. Technol. 217 (2025) 182–220.
[17] G. Di Liberto, L.A. Cipriano, S. Tosoni, G. Pacchioni, Chem Eur J 27 (2021) 13306–13317.
[18] H. Li, H. Yu, X. Quan, S. Chen, H. Zhao, Adv. Funct. Mater. 25 (2015) 3074–3080.
[19] T.L. Madanu, S.R. Mouchet, O. Deparis, J. Liu, Y. Li, B.-L. Su, J. Colloid Interface Sci. 634 (2023) 290–299.
[20] G. Odling, N. Robertson, ChemPhysChem 17 (2016) 2872–2880.
[21] M. Xie, X. Fu, L. Jing, P. Luan, Y. Feng, H. Fu, Adv. Energy Mater. 4 (2014) 1300995.
[22] T.L. Madanu, L. Chaabane, S.R. Mouchet, O. Deparis, B.-L. Su, J. Colloid Interface Sci. 647 (2023) 233–245.
[23] X. Wang, X. Li, J. Low, RSC Adv. 11 (2021) 8751–8758.
[24] M. Wu, J. Jin, J. Liu, Z. Deng, Y. Li, O. Deparis, B.-L. Su, J. Mater. Chem. A 1 (2013) 15491–15500.
[25] H. Xiang, S. Yang, E. Talukder, C. Huang, K. Chen, Inorganics 11 (2023) 337.
[26] J. Liu, J. Jin, Y. Li, H.-W. Huang, C. Wang, M. Wu, L.-H. Chen, B.-L. Su, J. Mater. Chem. A 2 (2014) 5051–5059.
[27] G. Collins, A. Lonergan, D. McNulty, C. Glynn, D. Buckley, C. Hu, C. O'Dwyer, Adv. Mater. Interfaces 7 (2020) 1901805.
[28] J.I. Chen, G. von Freymann, S.Y. Choi, V. Kitaev, G.A. Ozin, Adv. Mater. 18 (2006) 1915–1919.
[29] J. Zhang, X. Cai, X. Fu, D. Teng, G. Murtaza, Z. Meng, Z. Jia, L. Qiu, ACS Appl. Nano Mater. 7 (2024) 15376–15386.
[30] A. Lonergan, C. Hu, C. O'Dwyer, Phys. Rev. Mater. 4 (2020) 065201.
[31] K. Yee, IEEE Trans. Antennas Propag. 14 (1966) 302–307.
[32] D. Gaillot, T. Yamashita, C. Summers, Phys. Rev. B 72 (2005) 205109.
[33] O. Deparis, L. Wéber, Numerical predictions of the improvement of solar energy harvesting in inverse opal photonic crystals by tuning the slow light effect to higher photonic bands, SPIE Conference 13608 Photonic Fiber and Crystal Devices: Advances in Materials and Innovations in Device Applications XIX, San Diego (USA), 2025.
[34] Y.R. Park, K.J. Kim, Thin Solid Films 484 (2005) 34–38.
[35] Y. Yuan, Y. Huang, F. Ma, Z. Zhang, X. Wei, J. Mater. Sci. 52 (2017) 8546–8555.
[36] M. Wang, W. Li, Y. Zhao, S. Gu, F. Wang, H. Li, X. Liu, C. Ren, RSC Adv. 6 (2016) 75482–75490.
[37] K. Drisya, M. Solís-López, J. Ríos-Ramírez, J. Durán-Álvarez, A. Rousseau, S. Velumani, R. Asomoza, A. Kassiba, A. Jantrania, H. Castaneda, Sci. Rep. 10 (2020) 13507.
[38] O. Deparis, S. Mouchet, L. Dellieu, J.-F. Colomer, M. Sarrazin, Mater. Today Proc. 1 (2014) 122–129.
[39] M. Moharam, T.K. Gaylord, J. Opt. Soc. Am. 71 (1981) 811–818.
[40] O. Deparis, S. Mouchet, B.-L. Su, Phys. Chem. Chem. Phys. 17 (2015) 30525–30532.
[41] M. Curti, G. Zvitco, M.A. Grela, C.B. Mendive, Chem. Phys. 502 (2018) 33–38.
[42] C. Sirisamphanwong, C. Sirisamphanwong, Energy Procedia 34 (2013) 430–438.
[43] X. Zhang, S. John, Opt. Express 29 (2021) 22376–22402.
[44] M. Ploydaeng, N. Rajatanavin, P. Rattanakaemakorn, Photodermatol. Photoimmunol. Photomed. 37 (2021) 12–19.
[45] H.A. Foster, I.B. Ditta, S. Varghese, A. Steele, Appl. Microbiol. Biotechnol. 90 (2011) 1847–1865.
[46] N. Bono, F. Ponti, C. Punta, G. Candiani, Materials 14 (2021) 1075.
[47] Y. Wei, H. Meng, Q. Wu, X. Bai, Y. Zhang, Catalysts 13 (2023) 1466.
[48] J. Yu, A. Caravaca, C. Guillard, P. Vernoux, L. Zhou, L. Wang, J. Lei, J. Zhang, Y. Liu, Catalysts 11 (2021) 464.
[49] S. Loukopoulos, E. Sakellis, M.G. Kostakis, D.-T. Gerokonstantis, P. Tsipas, S. Gardelis, A.G. Kontos, F.K. Katsaros, Z. Sideratou, G.E. Romanos, ACS Omega 8 (2023) 33639–33650.
[50] J.A. Lai, J. Xu, J. Wang, Z. Zhang, Y. Zhang, L. Wang, ChemCatChem 16 (2024) e202400961.
[51] D.M. Tobaldi, D. Dvoranová, L. Lajaunie, N. Rozman, B. Figueiredo, M.P. Seabra, A.S. Škapin, J.J. Calvino, V. Brezová, J.A. Labrincha, Chem. Eng. J. 405 (2021) 126651.
[52] S. Bonetta, S. Bonetta, F. Motta, A. Strini, E. Carraro, AMB Express 3 (2013) 1–8.
[53] M. Tanveer, G.T. Guyer, G. Abbas, Water Environ. Res 91 (2019) 822–829.
[54] N. Jafari, K. Ebrahimpour, A. Abdolahnejad, M. Karimi, A. Ebrahimi, J. Environ. Health Sci. Eng. 17 (2019) 1171–1183.
[55] M. Wu, J. Liu, J. Jin, C. Wang, S. Huang, Z. Deng, Y. Li, B.-L. Su, Appl. Catal. B. 150 (2014) 411–420.
[56] M. Tayebi, B.-K. Lee, Renew. Sustain. Energy Rev. 111 (2019) 332–343.
[57] H. Hou, L. Wang, F. Gao, X. Yang, W. Yang, J. Mater. Chem. C 7 (2019) 7858–7864.
[58] S. Sun, P. Gao, Y. Yang, P. Yang, Y. Chen, Y. Wang, ACS Appl. Mater. Interfaces. 8 (2016) 18126–18131.
[59] J. Muller, A. Herman, A. Mayer, O. Deparis, Opt. Express 23 (2015) A657–A670.